


國 立 交 通 大 學

電子工程學系 電子研究所

博 士 論 文

集極相關製程及結構對於 0.18 微米世代之  
矽鍺異質接面雙極性電晶體直流及射頻效  
能影響的物理機制分析以及銅製程相容低  
介電常數材質之電性強化技術開發



*A study and Analysis of the Impacts on the DC and RF  
characteristics of 0.18  $\mu\text{m}$  SiGe HBT Resulting from the  
Collector Associated Processes and Doping Profiles and  
Copper Comparable Technology Development for Improving  
the Performance of the Low-K Material*

研究生：曾明豪

Ming-Hau Tseng

指導教授：張國明 教授 Dr. Kow-Ming Chang

中華民國九十三年六月

集極相關製程及結構對於 0.18 微米世代之矽鍺異質接面  
雙極性電晶體直流及射頻效能影響的物理機制分析以及銅

製程相容低介電常數材質之電性強化技術開發

A study and Analysis of the Impacts on the DC and RF  
characteristics of 0.18  $\mu\text{m}$  SiGe HBT Resulting from the  
Collector Associated Processes and Doping Profiles and Copper  
Comparable Technology Development for Improving the  
Performance of the Low-K Material

研究生：曾明豪

**Student : Ming Hau Tseng**

指導教授：張國明 博士

**Adviser : Dr. Kow Ming Chang**



國立交通大學

電子工程學系 電子研究所

博士論文

A Dissertation

Submitted to Institute of Electronics  
College of Electrical Engineering and Computer Science

National Chiao Tung University

In Partial Fulfillment of Requirements

For the Degree of Doctor of Philosophy

In

Electronics Engineering

May 2004/4/24 Hsinchu, Twiwan, Republic of China

中華民國九十三年五月

集極相關製程及結構對於 0.18 微米世代之矽鍺異質接面雙  
極性電晶體直流及射頻效能影響的物理機制分析以及銅製  
程相容低介電常數材質之電性強化技術開發

研究生：曾明豪

指導教授：張國明 博士

國立交通大學

電子工程學系 電子研究所

博士論文



本論文主要內容是針對矽鍺異質接面雙極性電晶體 (SiGe HBT) 之直流及射頻行為與其原件之參雜分佈及製造過程之間的關係作深入的研究探討。

首先,本研究設計了一套估算電晶體 transit time 的方式此方式經過實際量測的結果驗證後證實具有一定的準確度.可以在元件設計階段,以製程參數為基礎,定性評估電晶體的高頻效能.除此之外,可解析 transit time 的各個組成成分比例,可以幫助元件設計者深入了解元件的特質,以最有效最省資源的方式發展。

其次,確立了 SiGe HBT 電晶體中集極參雜濃度對基極電阻的調變作用,並證實其物理機制.此外更進一步證實 SiGe HBT 的射頻行為中  $f_T$  及  $f_{max}$  的峰值不發生

在同一壓電流密度值上的這個現象,其背後的原因是基極電阻的調變作用所引起.

除此之外,本研究亦提出這個現象對電路設計的影響及潛在困難,並提出建議.

再者,是針對深溝結構對 SiGe HBT 電晶體的直流及射頻特性的影響的研究.

深溝結構是類比及射頻應用中常用的技術作為阻隔電路中訊號的洩漏.但是很少有研究針對深溝結構對元件的直流及射頻特性的影響提出報告.本研究發現,深溝結構製程確實對直流及射頻特性有所調變,並對其相關物理機制及電性影響有深入的研究與探討.

此外,本研究中發展了一個以  $\text{NH}_3$  電漿處理低介電電材料的製程,能降低低介電材料在灰化的過程中所遭受的破壞.除此之外,這一個處理方式同時可抑制銅在低介電材料中的擴散.本方法是一個有效,經濟而且符合製程整合要素的方法.最後,本研究針對接面可變電容之直流及射頻特性對元件幾何的變化作分析.

這部分研究結果將對訊號生電路的設計者有相當程度的參考價值

**A study and Analysis of the Impacts on the DC and RF  
characteristics of 0.18  $\mu\text{m}$  SiGe HBT Resulting from the Collector  
Associated Processes and Doping Profiles and Copper Comparable  
Technology Development for Improving the Performance of the  
Low-K Material**

**Student** : Wen-Chih Yang

**Adviser** : Dr. Kow-Ming Chang

Department of Electronics Engineering & Institute of Electrics

National Chiao Tung University



In this research, the impacts and corresponding physical origins on the DC and RF characteristics of modern silicon germanium hetero-junction bipolar transistor related to the collector processes and doping profile have been studied.

First, a new and efficient transit time estimation approach has been developed and identified. By using this approach, the components which consisted the transit time of the transistor and could be difficultly decoupled in the simulation way could be obtained based on the doping profiles of the device. Such approach did great help during the device development steps because of its simple, fairly accurate and

efficient. Besides, the device designer could optimize the doping profile according to pre-estimation of the transit time components for improving the capability of the devices. Furthermore, after analyzing, it was discovered that the collector doping profile could be more important as the vertical dimension of the device continuously shrinking.

Second, the physics associated with the modulation behavior of the current flux distribution in the pinch base region has been studied. It was found that Such current distribution modulation was directly related to the doping concentration level in the collector region. Besides, it was also found that such behavior could also alter the bias dependency of the base resistance  $r_{B-I_C}$ . Furthermore, such altered  $r_{B-I_C}$  behavior has also been proven in this research that it should attribute to the inconsistency of the current density levels on which the peak cutoff frequency and maximum oscillation frequency took place.

Third, the associated physical origins and impacts from the deep trench process on the DC and RF characteristics of the SiGe HBT was investigated. For identifying the physical mechanism, several work have been done including the process simulation and practical measurement. It was proven that the key indexes of the HBT devices for circuit design including the RF noise characteristics and two-tone performance could be impacted. Such impact could be suppressed by increasing the collector doping

level.

Furthermore, a new-developed technology for improving the electric and physical performance of low-K material by  $\text{NH}_3$  plasma pre-treatment has been reported.

Finally, the DC and RF characteristics of the junction varactor respective to the geometry effect have been described which could be very valuable for the circuit designers in signal generation networks.



## 誌謝

首先我要對於我的指導教授 張國明博士致上我最崇高的敬意與謝意. 對於他多年來的指導與教誨, 使本人在學術研究上獲益良多, 同時也從老師身上學到許多待人處事的道理. 是我有生以來最寶貴的際遇.

另外我要感謝我的父母, 曾勝雄先生, 呂淑英女士的全力支持, 此外要感謝我的家人以及好友張美雯小姐在精神上的支持及鼓勵.





# Contents

Chinese Abstract.....	i
English Abstract.....	iii
Acknowledgements.....	vi
Contents.....	vii
Table Captions.....	x
Figure Captions.....	xii
Chapter 1 Introduction .....	1
Chapter 2 Study on Forward Transient Time Distribution and Cutoff Frequency for HBT Devices.....	5
2.0 Associated Physics.....	5
2.1 Transit Time Distribution.....	14
2.2 Geometry Dependency of Cutoff Frequency.....	18
2.3 Device Characteristics on Epitaxy thickness Effect.....	20
2.4 Conclusion.....	22
Appendix A.2.....	22
References.....	25
Figures and Tables in Chapter 2.....	28
Chapter 3 Modulation on Current Distribution in the Pinched Base Region Corresponding to Collector Doping Profiles and the Correlated Impacts in DC and RF Characteristics.....	51
3.0 Introduction.....	52
3.1 Current Dependency of the Base Resistance.....	53
3.2 Associated Physics: Current Spreading and Crowding.....	58
3.3 Physics Deductions, Simulations and Identifications.....	61

3.4 Impacts on Cutoff Frequency and maximum Oscillation Frequency.....	64
3.5 Mathematical Verifications.....	65
3.6 Conclusion.....	68
References.....	69
Figures and Tables in Chapter 3.....	71
<b>Chapter 4 Impacts of DC and RF Characteristics from the Association of Collector Doping Profiles and Deep Trench Structure.....</b>	<b>100</b>
4.0 Associated Physics.....	101
4.1 RF Characteristics of Deep Trench and Non-deep Trench Devices.....	102
4.2 RF Noise Characteristics of Deep Trench and Non-deep Trench Devices.....	105
4.2.1 Impacts on Minimum Noise Figure and Associated Gain.....	105
4.2.2 Impacts on Optimum Source Matching Point $\Gamma_{opt}$ .....	107
4.2.3 Impacts on Device S Parameters.....	109
4.3 Linearity and Power Capability of Deep Trench and Non-deep Trench Devices.....	111
4.3.1 DT Associated Impacts on TOI.....	111
4.3.2 DT Associated Impacts on $G_p$ and PAE.....	112
4.4 Conclusion.....	113
References.....	114
Figures and Tables in Chapter 4.....	115
<b>Chapter 5 Electrical and Physical Characteristics Improvement of Low-K Dielectric by <math>NH_3</math> Plasma Pre-treatment.....</b>	<b>138</b>

5.1 Introduction.....	138
5.2 Experiments.....	140
5.3 Results and Discussions.....	141
5.4 Conclusion.....	145
References.....	146
Figures and Tables in Chapter 5.....	149
Chapter 6 Conclusion and Future Works.....	159



# Table Captions

## Chapter 2

Table 2.1.1 The list of the transit time and the corresponding compositions of the SiGe HBT with  $1 \times 0.2 \times 10 \mu\text{m}^2$  area under  $V_{\text{BC}}$  1 volt and  $I_{\text{C}}$  about 12 mA.

## Chapter 3

Table 3.1. Devices name-list mapping with the corresponding doping profiles and geometries.

Table 3.2 Emitter resistance of SiGe HBT devices in various geometry

Table 3.3 (a) Parameters involved in estimating  $f_{\text{max\_meas}}$  illustrating in Fig. 6 (a)

Table 3.3 (b) Parameters involved in estimating  $f_{\text{max\_meas}}$  illustrating in Fig. 6 (b)

Table 3.3 (c) Parameters involved in estimating  $f_{\text{max\_meas}}$  illustrating in Fig. 6 (c)



# Figure Captions

## Chapter 2

Figure 2.0.1 The high frequency small signal model of SiGe HBT.

Figure 2.0.2 The schematic cross-section of view of SiGe HBT with deep trench isolation structure.

Figure 2.0.3 Schematic illustration of the traditional approaches to extract forward transit time by the bias current dependent relationship of the inverse of the cutoff frequency.

Figure 2.0.4 Process flow of SiGe HBT fabricated by the BiCMOS technology.

Figure 2.0.5 (a) Schematic illustration of the doping profile of a bipolar transistor.

Figure 2.0.5 (b) Minority carrier distribution and the associated field distribution for transit time estimation.

Figure 2.1.1 (a) Output characteristics of a SiGe HBT with  $1 \times 0.2 \times 10 \mu\text{m}^2$  area.

Figure 2.1.1 (b) Gummel Plot of a SiGe HBT with  $1 \times 0.2 \times 10 \mu\text{m}^2$  area. And the current gain  $\beta$  is about 100.

Figure 2.1.2 (a) Input reflection coefficient  $S_{11}$  and output reflection coefficient  $S_{22}$  of a SiGe HBT with  $1 \times 0.2 \times 10 \mu\text{m}^2$  area under  $V_{BC}$  1 volt and  $V_{BE}$  from 0.75 to 1.4 Volt.

Figure 2.1.2 (b) Small signal current gain  $h_{FE}$  of a SiGe HBT with  $1 \times 0.2 \times 10 \mu\text{m}^2$  area under  $V_{BC}$  1 volt and  $I_c$  about 12 mA. The extracted cutoff frequency is about 120 GHz.

Figure 2.1.3 (a) Bias dependency of  $f_T$  of a SiGe HBT with  $1 \times 0.4 \times 10 \mu\text{m}^2$  area under  $V_{BC}$  1 volt. The peak value of  $f_T$  takes place near  $I_c = 10$  mA and the corresponding current density is denoted as  $J_k$ .

Figure 2.1.3 (b) Measurement results of  $1/f_T$  vs.  $1/I_c$  of a SiGe HBT with  $1 \times 0.2 \times 10$ ,  $2 \times 0.2 \times 10$  and  $4 \times 0.2 \times 10 \mu\text{m}^2$  area under  $V_{BC}$  1 volt. The intersect value are 1.28, 1.42 and 1.68 ps, respectively.

Figure 2.2.1 The measured  $1/f_T$ - $1/I_c$  relationships of H-group SiGe HBT in  $1 \times 0.2 \times 10$  and  $2 \times 0.9 \times 10 \mu\text{m}^2$  with collector epitaxy thickness of  $0.5 \mu\text{m}$  under  $V_{BC}$  1 volt. The inserted figure is the corresponding  $f_T$ - $J_c$  plot

Figure 2.2.2 The schematic cross-section of H-group SiGe HBT device in (a) wider and (b) narrower emitter along with the current flux in the collector region.  $J_c$  and  $J_c'$  were denoted as the current density on the base-collector junction edges of the base and collector sides, respectively

Figure 2.3.1 The measured  $1/f_T$ - $1/I_c$  relationships of (a) H-group and (b) L-group SiGe HBT devices in fixed  $4 \times 0.2 \times 10 \mu\text{m}^2$ , and collector epitaxy thickness of  $0.5$

and  $1\ \mu\text{m}$  under  $V_{\text{BC}}\ 1\ \text{volt}$ . The inserted figure is the corresponding  $f_{\text{T}}\text{-}J_{\text{C}}$  plot

Figure 2.3.2 The schematic cross-section of L-group SiGe HBT device with (a) thinner and (b) thicker epitaxy collector along with the current flux in the collector region.  $J_{\text{c}}$  and  $J_{\text{c}}'$  were denoted as the current density on the base-collector junction edges of the base and collector sides, respectively

Figure 2.3.3 The measured  $f_{\text{T}}\text{-}J_{\text{C}}$  relationships of H and L-group SiGe HBT devices in  $1 \times 0.2 \times 10$  and  $1 \times 0.9 \times 10\ \mu\text{m}^2$  with collector epitaxy thickness of  $0.5\ \mu\text{m}$  under  $V_{\text{BC}}\ 1\ \text{volt}$ .

Figure 2.3.4 (a) The schematic cross-section of H-group SiGe HBT devices with (a) higher and (b) lower collector doping level along with the current flux in the collector region.  $J_{\text{c}}$  and  $J_{\text{c}}'$  were denoted as the current density on the base-collector junction edges of the base and collector sides, respectively

### Chapter 3

Figure 3.1 (a) Cross-section of 4-emitter SiGe HBT devices with SIC layer

Figure 3.1 (b) Top view of 4-emitter SiGe HBT.

Figure 3.1 (c) Schematic vertical doping profiles of SiGe HBT devices with the emitter, base and SIC layer doping concentrations of  $N_{\text{E}}$ ,  $N_{\text{B}}$  and  $N_{\text{SIC}}$ , respectively.

Figure 3.2 High frequency small signal model of SiGe HBT for  $f_{\text{T}}$  and  $f_{\text{max}}$  derivations.

Figure 3.3 (a) Base resistance  $r_{\text{B}}$  versus collector current density for HBT devices with fixed emitter lengths  $L_{\text{E}}$  yet various emitter widths  $W_{\text{E}}$ .

Figure 3.3 (b) Base resistance  $r_{\text{B}}$  versus collector current density for HBT devices with fixed emitter widths  $W_{\text{E}}$  yet various emitter lengths  $L_{\text{E}}$  and emitter strips  $N_{\text{E}}$ .

Figure 3.3 (c) Base resistance  $r_{\text{B}}$  versus collector current density for HBT devices with various doping profiles.

Figure 3.4 Schematic illustration of current flux distribution on relative low, moderate high and high biasing current conditions in the intrinsic base region of group (a) M and (b) H group devices.

Figure 3.4 (c) MEDICI simulation results of current density distribution profiles along the lateral direction  $x$  on the emitter-base junction edge and in the middle of poly-emitter structure under the current densities  $10^{-5}$ ,  $10^{-3}$ ,  $3 \times 10^{-3}$  and  $10^{-2}\ \text{A}/\mu\text{m}^2$ . The location  $x = 0$  were the emitter center.

Figure 3.4 (d) MEDICI simulation results of current density distribution profiles along the vertical direction  $y$  on the location of  $x = 0.13\ \mu\text{m}$  under the current densities  $10^{-5}$ ,  $10^{-3}$ ,  $3 \times 10^{-3}$  and  $10^{-2}\ \text{A}/\mu\text{m}^2$ . The location  $x = 0$  were the emitter center.

Figure 3.4 (e) Schematic cross-section of base-emitter junction with current flux distribution from emitter to base under relative low voltage (e)  $V_{BE1}$  and (f)  $V_{BE2}$ .

Figure 3.4 (g) Status illustrations of the diodes in figure 4 (e) and (f) under various bias conditions.

Figure 3.4 (h) Illustrations of the vertical current distribution in base-emitter region under  $V_{BE1}$  and  $V_{BE2}$ .

Figure 3.5 (a) Current dependency of cutoff frequency  $f_T$  and corresponding maximum oscillation frequency  $f_{max}$  of HBT devices with fixed emitter widths in  $0.2 \mu\text{m}$  and lengths in  $10.16 \mu\text{m}$  yet various emitter numbers.

Figure 3.5 (b) Current dependency of cutoff frequency  $f_T$  and corresponding maximum oscillation frequency  $f_{max}$  of HBT devices with fixed emitter lengths yet various emitter widths.

Figure 3.5 (c) Current dependency of cutoff frequency  $f_T$  and corresponding maximum oscillation frequency  $f_{max}$  of HBT devices with fixed emitter lengths and widths yet various doping profiles.

Figure 3.6 Current dependency of measured cutoff frequency  $f_{T\_meas}$  and extracted base resistance  $r_B$  along with measured and estimated maximum oscillation frequency  $f_{max\_meas}$  and  $f_{max\_cal}$  of devices (a) H\_113 (b) M\_115 (c) L\_111

## Chapter 4

Figure 4.0.1 Schematic base-collector junction of SiGe HBT with the doping profile and the carrier fluxes under (a) low and (b) high current injection regime.

Figure 4.1.1 Measured result of the cutoff frequency and maximum oscillation frequency of DT and NDT SiGe HBT devices of H, M and L-groups in  $2 \times 0.2 \times 10 \mu\text{m}^2$  versus collector current density under  $V_{BC}$  1 volt.

Figure 4.1.2 Measured result of the base-collector capacitance and breakdown voltage of DT and NDT SiGe HBT devices of H, M and L-groups in  $2 \times 0.2 \times 10 \mu\text{m}^2$  versus collector current density under  $V_{BC}$  1 volt.

Figure 4.1.3 T-SUPREM 4 simulation results of the doping concentration profiles of As, P and total n-type carriers of DT and NDT devices in D and H groups. The original position  $0 \mu\text{m}$  was the BC junction edge on the collector side. The inserted figure illustrated the enlarged version between  $x = 0$  and  $0.2 \mu\text{m}$ .

Figure 4.2.1 The frequency dependency of the minimum noise figure and associated gain of DT and NDT SiGe HBT devices of H and L-groups in  $2 \times 0.2 \times 10 \mu\text{m}^2$  under  $V_{BE}$  (a) 0.85 and (b) 0.9 volt and  $V_{BC}$  1 volt.

Figure 4.2.1 The bias dependency of the minimum noise figure and associated gain of DT and NDT SiGe HBT devices of H and L-groups in  $2 \times 0.2 \times 10 \mu\text{m}^2$  versus

collector current under  $V_{BC}$  1 volt at (c) 2.4 and (d) 5.8 GHz

Figure 4.2.2 The frequency dependency of the magnitude and angle of the optimum source matching point  $\Gamma_{opt}$  of DT and NDT SiGe HBT devices of H and L-groups in  $2 \times 0.2 \times 10 \mu\text{m}^2$  under  $V_{BE}$  (a) 0.85 and (b) 0.9 volt and  $V_{BC}$  1 volt.

Figure 4.2.2 The bias dependency of the magnitude (Upper) and angle (Lower) of the optimum source matching point  $\Gamma_{opt}$  of DT and NDT SiGe HBT devices of H and L-groups in  $2 \times 0.2 \times 10 \mu\text{m}^2$  versus collector current under  $V_{BC}$  1 volt at (c) 2.4 and (d) 5.8 GHz

Figure 4.2.3 The frequency dependency of the optimum source matching point  $\Gamma_{opt}$  and output reflection coefficient  $S_{22}$  of DT and NDT SiGe HBT devices of H and L-groups in  $2 \times 0.2 \times 10 \mu\text{m}^2$  under  $V_{BE}$  (a) 0.85 and (b) 0.9 volt and  $V_{BC}$  1 volt.

Figure 4.2.3 The frequency dependency of the forward transmission coefficient  $S_{21}$  and input reflection coefficient  $S_{11}$  of DT and NDT SiGe HBT devices of H and L-groups in  $2 \times 0.2 \times 10 \mu\text{m}^2$  under  $V_{BE}$  (c) 0.85 and (d) 0.9 volt and  $V_{BC}$  1 volt.

Figure 4.3.1 The bias dependency of the two-tone third order intersect point (TOI) of DT and NDT SiGe HBT devices of H and L-groups in  $2 \times 0.2 \times 10 \mu\text{m}^2$  versus collector current under  $V_{BC}$  1 volt at (a) 2.4 and (b) 5.8 GHz. The adjacent channel offset is 1 MHz.

Figure 4.3.2 The input power dependency of the power gain ( $G_p$ ) and power added efficiency (PAE) of DT and NDT SiGe HBT devices of H and L-groups in  $2 \times 0.2 \times 10 \mu\text{m}^2$  under (a)  $V_{BE}$  0.85 and  $V_{BC}$  1 volt at 2.4 GHz (b)  $V_{BE}$  0.85 and  $V_{BC}$  1 volt at 5.8 GHz (c)  $V_{BE}$  0.9 and  $V_{BC}$  1 volt at 2.4 GHz (d)  $V_{BE}$  0.9 and  $V_{BC}$  1 volt at 5.8 GHz.

## Chapter 5

Figure 5.1.1 FTIR spectra of the different pre-treated X-720 films after  $O_2$  plasma treatment (ashing) for 10 min.

Figure 5.1.2 The thickness and the dielectric constant variation of the different pre-treated X-720 films after  $O_2$  plasma treatment (ashing) for 10 min..

Figure 5.1.3 XPS spectra of the X-720 film before and after  $NH_3$  plasma pre-treatment.

Figure 5.1.4  $C_{1s}$  XPS spectra of the different pre-treated X-720 films (a) before and (b) after  $O_2$  plasma treatment (ashing) for 10 min.

Figure 5.1.5 The SEM pictures of (a) as-cured, (b) as-cured sample after  $O_2$  plasma treatment (ashing) for 10 min, (c)  $NH_3$  plasma pre-treated sample after  $O_2$  plasma treatment (ashing) for 10 min.



Figure 5.1.6 Comparing the leakage current density of the different pre-treated X-720 samples before and after O<sub>2</sub> plasma treatment (ashing) for 10 min.

Figure 5.1.7 The leakage current density of (a) as-cured and (b) NH<sub>3</sub> plasma pre-treated X-720 samples after annealing at 350 and 400 for 1 hour.

Figure 5.1.8 Weibull plot of electrical breakdown field (E<sub>BD</sub>) distributions for as-cured and NH<sub>3</sub> plasma pre-treated X-720 films as the capacitor dielectric layers after different thermal treatment conditions.

